

## ARTICLE OPEN



# Spatial functional mapping of hypoxia inducible factor heterodimerisation and immune checkpoint regulators in clear cell renal cell carcinoma

Elena Safrygina<sup>1,2</sup>, Christopher Applebee<sup>1</sup>, Alan McIntyre<sup>3,4</sup>, Julian Padget<sup>2,4</sup>✉ and Banafshé Larijani<sup>1,4</sup>✉

© The Author(s) 2024, corrected publication 2024

**BACKGROUND:** Clear cell renal cell carcinoma (ccRCC) is a highly malignant subtype of kidney cancer. Ninety percent of ccRCC have inactivating mutations of VHL that stabilise transcription factors, HIF1 $\alpha$  and HIF2 $\alpha$ , only stabilised in hypoxia. The varied response to HIF2 inhibition, in the preclinical and clinical settings, suggests that assessment of HIF2 $\alpha$  activation state, not just expression levels is required as a biomarker of sensitivity to enable optimal clinical use.

**METHODS:** Two-site amplified time-resolved Förster Resonance Energy Transfer (aiFRET), with FRET-Efficiency, *E<sub>f</sub>*, as its read out, provides functional proteomics quantification, a precise step forward from protein expression as a tool for patient stratification. To enhance the clinical accessibility of *E<sub>f</sub>*, we have devised a new computational approach, Functional Oncology map (FuncOmap).

**RESULTS:** FuncOmap directly maps functional states of oncoproteins and allows functional states quantification at an enhanced spatial resolution. The innovative contributions in FuncOmap are the means to co-analyse and map expressional and functional state images and the enhancement of spatial resolution to facilitate clinical application. We show the spatial interactive states HIF2 $\alpha$  and HIF1 $\beta$  in ccRCC patient samples.

**CONCLUSION:** FuncOmap can be used to quantify heterogeneity in patient response and improve accurate patient stratification, thus enhancing the power of precision.

BJC Reports; <https://doi.org/10.1038/s44276-023-00033-7>

## BACKGROUND

Clear cell renal cell carcinoma (ccRCC) is a highly malignant subtype of kidney cancer that represents 80% of 13,100 kidney cancer diagnosed in the UK each year (CRUK). ccRCC are treated with molecular-targeted therapeutics that inhibit immune checkpoints, tyrosine kinases and HIF2 $\alpha$  [1]. Responses are heterogeneous and a lack of adequate biomarkers to identify the right drug for the right patient is preventing precision medicine for these patients leading to treatment with costly, toxic therapeutics that might not work. HIF2 $\alpha$  is a key target for ccRCC [2–5], and the FDA recently approved a HIF2 $\alpha$  inhibitor, Belzutifan, which has an overall response rate of 49% in Von Hippel-Lindau (VHL) mutant ccRCC [6]. Ninety per cent of ccRCC have inactivating mutations of VHL [2, 3]. VHL mutations stabilise transcription factors, HIF1 $\alpha$  and HIF2 $\alpha$ , that are normally only stabilised in hypoxia [7]. Belzutifan prevents HIF2 $\alpha$  from dimerising with HIF1 $\beta$ , thereby preventing HIF2 $\alpha$  transcriptional activity [4]. Preclinical studies investigating sensitivity to Belzutifan suggest that activation state and not expression per se is a key determinant of response [5, 8]. The varied response to HIF2 $\alpha$  inhibition suggests that assessment of HIF2 $\alpha$  activation state (binding to HIF1 $\beta$ ), not just expression levels could serve as a biomarker to optimise clinical use [8].

ccRCC patients show improved survival following treatment with immune checkpoint inhibitors (ICI) targeting CTLA-4 and PD-1 (Ipilimumab/Nivolumab) [9, 10]. Combination Immune checkpoint and HIF2 $\alpha$  targeting clinical trials are underway (Belzutifan/Pembrolizumab) (clinicaltrials.gov). Indeed, immune checkpoint regulators are modulated differently by HIF2 $\alpha$  versus HIF1 $\alpha$  [10]. Therefore, mechanistically understanding the engagement of HIF2 $\alpha$  with HIF1 $\beta$  and the impact that this has on immune checkpoint interactions is key to understanding appropriate patient selection for therapeutic modalities. Accurate patient stratification remains a key factor for optimising both HIF2 $\alpha$  inhibitors and ICI.

Improving patient stratification will unleash the power of precision medicine, identifying those most likely to respond. A key problem is the precise selection of the right treatment for each individual patient. The use of expression levels of oncoproteins rather than their activation/interaction states (how they function and interact with other proteins) in therapy/patient selection is imprecise, because expression levels of proteins poorly correlate with an accurate prognosis, whereas the analysis of functional states does [11, 12].

Our approach to enhance precision is to use quantitative molecular imaging. We have harnessed a two-site amplified time

<sup>1</sup>Cell Biophysics Laboratory, Centre for Therapeutic Innovation, Life Science Department, University of Bath, Claverton Down, Bath BA2 7AY, UK. <sup>2</sup>ART-AI, Department of Computational Sciences, University of Bath, Claverton Down, Bath BA2 7AY, UK. <sup>3</sup>Centre for Cancer Sciences, School of Medicine, Biodiscovery Institute, Science Road, University of Nottingham, NG7 2RD Nottingham, UK. <sup>4</sup>These authors contributed equally: Alan McIntyre, Julian Padget, Banafshé Larijani. ✉email: [masjap@bath.ac.uk](mailto:masjap@bath.ac.uk); [bl666@bath.ac.uk](mailto:bl666@bath.ac.uk)

Received: 7 September 2023 Revised: 13 December 2023 Accepted: 20 December 2023

Published online: 09 February 2024

resolved Förster Resonance Energy Transfer (aFRET-intracellular and iFRET-intercellular-aiFRET) method, which is detected by multiple frequency domain fluorescence lifetime imaging microscopy (mFLIM). Time-resolved FRET is used to measure molecular distances quantifying protein-protein interactions between 1–10 nm. aiFRET provides spatial functional proteomics quantification resulting in a significant and precise step forward from protein levels as a tool for patient stratification.

However, the exploitation of aiFRET has proven to be difficult in the clinical arena. The readout, until recently for functional states of proteins (interactive states or conformational changes due to posttranslational modifications) has been FRET efficiency ( $E_f$ ), where we have shown heterogeneity of  $E_f$  via box and whisker plots. Although the quantification has been very precise, the localisation of the  $E_f$  from the box and whisker plots on the tissue sections or individual TMA cores remains obscure.

To overcome this limitation and increase the clinical accessibility of aiFRET in this study, we have devised a new algorithm whereby  $E_f$  values can be directly calculated from the lifetime images and mapped on to the expression level (fluorescent) image of the oncoproteins under investigation. Our new methodology, Functional Oncology Map (FuncOmap), not only is a direct spatial mapping of the functional states of oncoproteins but also allows per-pixel determination of these functional states. Here, we show the differences in analyses between determining the functional state variations via the traditional box and whisker plots and the new direct spatial functional state determination via FuncOmap. We show for the first time that we can determine HIF2 $\alpha$  and HIF1 $\beta$  interactive states in colorectal single cells and patient ccRCC samples. Furthermore, we show that the immune check point regulators (PD-1/PDL-1) interactive states can be determined via FuncOmap in the same ccRCC TMAs. FuncOmap enhances precision and automatically, via the new algorithm, locates  $E_f$  on the expression state of the HIF2 $\alpha$  and PD-1 in this specific case study. This enables spatial resolution relationships of protein interactions to be identified. FuncOmap can in principle also be used as a general tool for determining the per-pixel functional states of proteins in any type of pathology and not only oncology.

## MATERIALS AND METHODS

### Antibodies and reagents

Recombinant HIF-2 $\alpha$  antibody and HIF-1 $\beta$  antibodies were purchased from Abcam (catalogue numbers ab243861 and ab2771 respectively). Monoclonal antibodies mouse anti-PD-1, rabbit anti-PD-L1 were purchased from Abcam (catalogue numbers ab52587 and ab205921 respectively). AffiniPure F(ab')<sub>2</sub> fragment donkey anti-mouse IgG (H + L) and peroxidase AffiniPure F(ab')<sub>2</sub> fragment donkey anti-rabbit IgG (H + L) were purchased from Jackson Immuno Research (catalogue numbers 715-006-150 and 711-036-152 respectively). Pierce endogenous peroxidase suppressor, TSA SuperBoost kit and Prolong Glass antifade mount were purchased from Thermo Fisher Scientific (catalogue numbers 35000, B40925 and P36980 respectively). ATTO488 NHS ester, bovine serum albumin and rhodamine B, were purchased from Sigma-Aldrich (catalogue numbers A2153-100G and 234141-10G respectively). LS174T- were purchased from ATCC. They were authenticated by STR. A commercial 24 core tissue microarray (TMA-KD241) was purchased from AMSBIO.

## METHODS

### Two-site assay for HIF-1 $\beta$ /HIF-2 $\alpha$ in colorectal cell lines (LS174T- ATCC)

The cells were tested for mycoplasma contamination seeded in eight well chambers to a confluence of 20%. They were incubated under normoxic and hypoxic conditions (1% O<sub>2</sub>, 48 h) prior to 4% PFA fixation at room temperature for 15 min. Washed twice with PBS and permeabilised with 0.01% TX-100 for 15 min. Followed by two washes with PBS. They were incubated for an hour at room temperature with 1% BSA (10 mg/ml). For the donor-only slides, they were incubated with either anti-PD-1 (at a dilution of

1:100) or anti-HIF-1 $\beta$  (at a dilution of 1:100). The donor-acceptor slides were treated with the following primary antibodies:  $\alpha$ PD-1 (1:100), or  $\alpha$ HIF-1 $\beta$  (1:100) and  $\alpha$ PD-L1 (1:500), or  $\alpha$ HIF-2 $\alpha$  (1:100). Primary antibodies were incubated overnight at 4 °C. Samples were washed with 0.02% PBST. The samples were treated with secondary F(ab')<sub>2</sub> fragments. F(ab')<sub>2</sub>-ATTO488 (at a dilution of 1:100) was introduced to the donor-only slides. As for the donor-acceptor slides, they received both F(ab')<sub>2</sub>-ATTO488 (1:100) and F(ab')<sub>2</sub>-HRP (1:200). These samples were incubated, for 2 h in the dark, at room temperature in a humidified container. After the incubation period slides were washed with 0.02% PBST. The donor-only slides were mounted with 1 drop of Prolong Glass antifade mount. The donor-acceptor slides were subjected to tyramide signal amplification (TSA) (see below).

### Two-site assay for HIF-1 $\beta$ /HIF-2 $\alpha$ and PD-1/PD-L1

The TMAs underwent antigen retrieval process using the Envision Flex retrieval solution, pH 9. The Dako PT-Link system was utilised, where the slides were heated to 95 °C for 20 min. Using a PAP pen, an aqueous-repelling border was outlined around each tissue fragment. Pierce endogenous peroxidase suppressor was then applied to each specimen, and the slides were left to incubate for 30 min at 21 °C room within a humid-controlled environment.

The samples underwent two washes with PBS before being incubated for an hour at room temperature with 3% BSA (10 mg/ml). For the donor-only slides, they were incubated with either anti-PD-1 (at a dilution of 1:100) or anti-HIF-1 $\beta$  (at a dilution of 1:100). The donor-acceptor slides were treated with the following primary antibodies:  $\alpha$ PD-1 (1:100), or  $\alpha$ HIF-1 $\beta$  (1:100) and  $\alpha$ PD-L1 (1:500), or  $\alpha$ HIF-2 $\alpha$  (1:100). Primary antibodies were incubated overnight at 4 °C. Samples were washed with 0.02% PBST. The samples were treated with secondary F(ab')<sub>2</sub> fragments. F(ab')<sub>2</sub>-ATTO488 (at a dilution of 1:100) was introduced to the donor-only slides. As for the donor-acceptor slides, they received both F(ab')<sub>2</sub>-ATTO488 (1:100) and F(ab')<sub>2</sub>-HRP (1:200). These samples were incubated, for 2 h in the dark, at room temperature in a humidified container. After the incubation period slides were washed with 0.02% PBST. The donor-only slides were mounted with 1 drop of Prolong Glass antifade mount.

The donor-acceptor slides were subjected to tyramide signal amplification (TSA). The purpose of tyramide signal amplification to amplify the acceptor labelling, thus increase the signal-to-noise ratio and enhancing resonance energy transfer. This procedure is described in detail in Veeriah et al. [12] and Sanchez-Magraner et al. [11]. The antibodies were labelled with species-specific F(ab')<sub>2</sub> fragments which were conjugated to ATTO488 (donor chromophore, used to label the receptor primary antibody) or HRP (used to label the ligand primary antibody). Tyramide signal amplification was used to conjugate the acceptor chromophore (Alexa594) to the HRP labelling the ligand [PCT/EP2018/062719 and PCT/GB14/050715].

### Time-resolved immune FRET (iFRET) determined by frequency-domain FLIM

The quantitative molecular imaging platform utilises a custom made semi-automated frequency-domain FLIM. The first slide (donor only) was excited by a modulated (40 MHz) diode 473 nm laser, and the lifetime of the donor alone recorded. The second slide was excited by the diode modulated 473 nm laser and lifetime of the donor in the presence of the acceptor recorded. The reduction of donor lifetime (caused by resonance energy transfer) due to the presence of the acceptor reports on distances of 1–10 nm and therefore acts as a “chemical ruler” enabling to quantify receptor-ligand and HIF protein interactions.

We identified the coincidence regions where both the donor and acceptor were observed. A total of 10–20 regions of interest (ROIs) were selected within this coincidence regions. Subsequently, the lifetimes, along with their corresponding standard deviations, were automatically obtained and exported to an Excel spreadsheet.

### Photophysical parameters for quantification of protein interactive states

As input the algorithm takes a lifetime image of donor in the presence of acceptor ( $\tau_{DA}$ ) and a lifetime image of the donor ( $\tau_D$ ), followed by calculation of reduction of  $\tau_{DA}$  compared to  $\tau_D$ , which is reflected in a metric called FRET-efficiency:

$$E_f = [1 - \langle \tau_{DA} \rangle / \langle \tau_D \rangle] \times 100 \quad (1)$$

FRET-efficiency is calculated as an average for each coincident region.

$Ef$  is directly related to the distance between the donor and acceptor fluorophores (Atto488 and Alexa 594) (Eq. (2)), where  $r$  is the distance between Atto488 and Alexa594 in these experiments. " $R_0$ " the Förster radius in this case is 5.83 nm and it is the distance whereby the transfer efficiency is 50%. A distance of 5.83 nm corresponds to 4% FRET-Efficiency. Therefore, the significant protein–protein (distance between the donor and acceptor) interactions are considered to be above 4%, indicated by the red line in on the box and whiskers plots:

$$Ef = \frac{R_0^6}{R_0^6 + r^6} \quad (2)$$

For each region of coincidence in the two-site assay, we computed the mean distance between the donor and the acceptor:

$$r = \sqrt[6]{R_0^6 * \frac{(1 - Ef)}{Ef}} \quad (3)$$

The application generates a table that summarises the quantitative characteristics for each coincident region. This includes the label, area, average FRET efficiency, and the mean distance between the donor and acceptor for each region.

Each overlapping region is colour-coded based on a colourmap that reflects a range from 0 to 50% FRET efficiency. This colour scale is used to create a heatmap, which is mapped automatically on the donor expression image.

### Statistics

The regression graphs for comparison of HIF-2 $\alpha$  expression levels with FRET-efficiency utilised Spearman regression to determine the  $r_s$  and  $p$  values. To evaluate FRET-efficiencies in two distinct experimental configurations (PD-1/PD-L1 and HIF-1 $\beta$ /HIF-2 $\alpha$ ), box and whisker plots were employed to visually represent the data from each TMA independently. This approach aimed to facilitate obtaining the graphs and comparison of FRET efficiency distributions among the group of patient samples from the commercial TMA. Following this, the Mann–Whitney  $U$  test was utilised to statistically analyse and compare the FRET efficiencies between ccRCC samples and the normal tissue. The null hypothesis presumes no significant difference between the two groups, while the alternative hypothesis poses a significant difference. The implementation of the Mann–Whitney  $U$ -test resulted in a  $p$  value. This  $p$  value signifies the likelihood of observing the differences in FRET efficiencies between the ccRCC and the adjacent normal tissue samples.

### Computational analysis of FuncOmap

The initial data are the images captured through a multiple frequency Fluorescence Lifetime Imaging Microscope (mfFLIM). There are two problems to solve from a user perspective: one is how to process that data to provide actionable clinical information, the other is how to enable clinicians to explore the data so they can confirm their diagnosis. We solved the first by constructing a false-colour composite image from the donor and donor/acceptor images which allows the clinician to observe levels of protein expression and protein function on the same image. We solved the second by making the image interactive so that mousing over the image displays additional data ( $Ef$ ) and molecular distance ( $r_{(nm)}$ ), while a drop-down control permits exploration of thresholding to shrink or grow the areas of protein function according to the measured  $Ef$ . From a computational perspective, the contributions are the choice and composition of the appropriate, validated library software, the construction of the image mapping between expressional and functional states and the spatial enhancement of the coincident image to highlight sites with significant levels of functional activation. The computational process, linked to the corresponding mathematics shown in the equations 1-3, appears in Fig. 1a.

The computational approach outlined in Fig. 1. is a significant advance on the existing method because it is automated—hence reproducible—more precise and provides whole sample functional information. As noted above, the initial data capture provides a donor and a donor-acceptor image because of the optical configuration. For each pixel we record the lifetime in the control donor and the donor/acceptor image and hence calculate the FRET efficiency, which provides the data to carry out a thresholding operation across the image and hence identify all the regions where protein function is above noise level. We use the Otsu thresholding method [13] to convert the original grey level expression

image into a binary one, where zeros represent the background and ones indicate regions where the proteins exist. To facilitate user exploration of the data, we provide a set of thresholds for user selection. After applying the threshold to the donor and donor/acceptor images, a logical “and” operation of the two pinpoints the coincident region where both proteins are present. Any pixels outside these overlapping regions are set to zero. Consequently, we identify the (image) coordinates of all coincident regions. Each region is assigned a label and the area it encompasses is calculated, represented as the total number of pixels within each specific coincident region. The “right” level for thresholding is an automatic function of the Otsu algorithm, which adapts to the image supplied to identify the best value to differentiate background from signal. This typically works out at a signal level 4 $\times$  that of the background but results in images where contrast is too low for human visual perception. This is resolved by increasing the contrast through multiplication of the signal up to 3-fold [12]. This factor only serves to assist human assessment of the images and does not affect the  $Ef$  or  $r_{(nm)}$  information in any way.

In contrast, the previous computational approach uses human annotation of the image to identify coincidence, then generates spreadsheets for donor and donor lifetime in the presence of acceptor. From these changes in lifetime the FRET efficiencies,  $Ef$  were calculated (Eq. (1)) and box and whisker statistical distributions plotted. The box and whisker plots provide an average across all the regions, which hides critical spatial localisation of protein activation states. Thus, the drawbacks here are the use of time-consuming human annotation, with attendant inaccuracy (marking regions using a mouse) and incompleteness (some regions that should be marked are not, not least because they can be too small for reliable and consistent identification), the homogenisation of the regions through the analysis process and the inaccessibility (to most clinicians) of a box and whiskers plot as a interpretable diagnostic tool.

The critique above notes that small regions are likely to missed with the manual approach. Small regions remain a problem, in the new approach—not in their detection; the thresholding automatically handles that—but in their presentation to the clinician, since a single pixel, for example, is still too small for ready identification on screen or selection by mouse. For this case, we have introduced a spatial enhancement in the rendering process that aggregates the pixels around one with a high  $Ef$ , in effect using homogenisation to reveal rather than hide information.

One of the main advantages of the new computational approach is that it allows for a one-step analysis, as opposed to multiple steps. In the new approach the lifetime changes,  $Ef$  and thresholding are all processed in an individual pixel. Furthermore, the computational complexity of the new approach is  $O(n)$ . Each step is linear in the dimensions of the image, since lifetime, FRET efficiency and thresholding all process individual pixels, while the aggregation process for spatial enhancement examines the eight pixels surrounding an individual pixel. The entire process is coded as a Python notebook that generates a web page for the presentation of the protein expression and functional state interactive map (Fig. 1a), from where the clinician can examine the different regions of coincidence by moving a mouse pointer over the image. As illustrated in Fig. 1b, the region selected has a pop-up that shows the data associated with the region and at the same time highlights the row in the data table. The clinician can also explore the effect of choosing different thresholds through the drop-down immediately below the image.

We demonstrate the application of the framework by mapping HIF1 $\beta$ /HIF2 $\alpha$  and PD-1/PD-L1 functional states (interaction) states on expression image of HIF1 $\beta$  and PD-1, respectively. The dataset is partitioned into two primary directories, one for the PD-1/PD-L1 experiment and the other for the HIF1 $\beta$ /HIF2 $\alpha$  experiment. Within each of these primary directories, seven separate sub-directories exist for each TMA: A1, A2, A5, B1, B5, and B7. These sub-directories contain image files, categorised into four types: Donor Expression, Donor Expression when an Acceptor is present, Donor Lifetime, and Donor Lifetime in the presence of an Acceptor.

FuncOmap allows for the visualisation of protein interaction states through a heatmap representation of average  $Ef$  within each coincidence region. By hovering over the heatmap, users can observe the  $Ef$  and distance  $r_{(nm)}$  between proteins in each region of interest (ROI). Additionally, this information can be shown as a spreadsheet, alongside the image, in the browser. Since FuncOmap is implemented on Google Colab, there is no requirement for additional software setup. Google Colab provides a certain amount of memory at no charge and all calculations are performed using cloud-based computational resources.

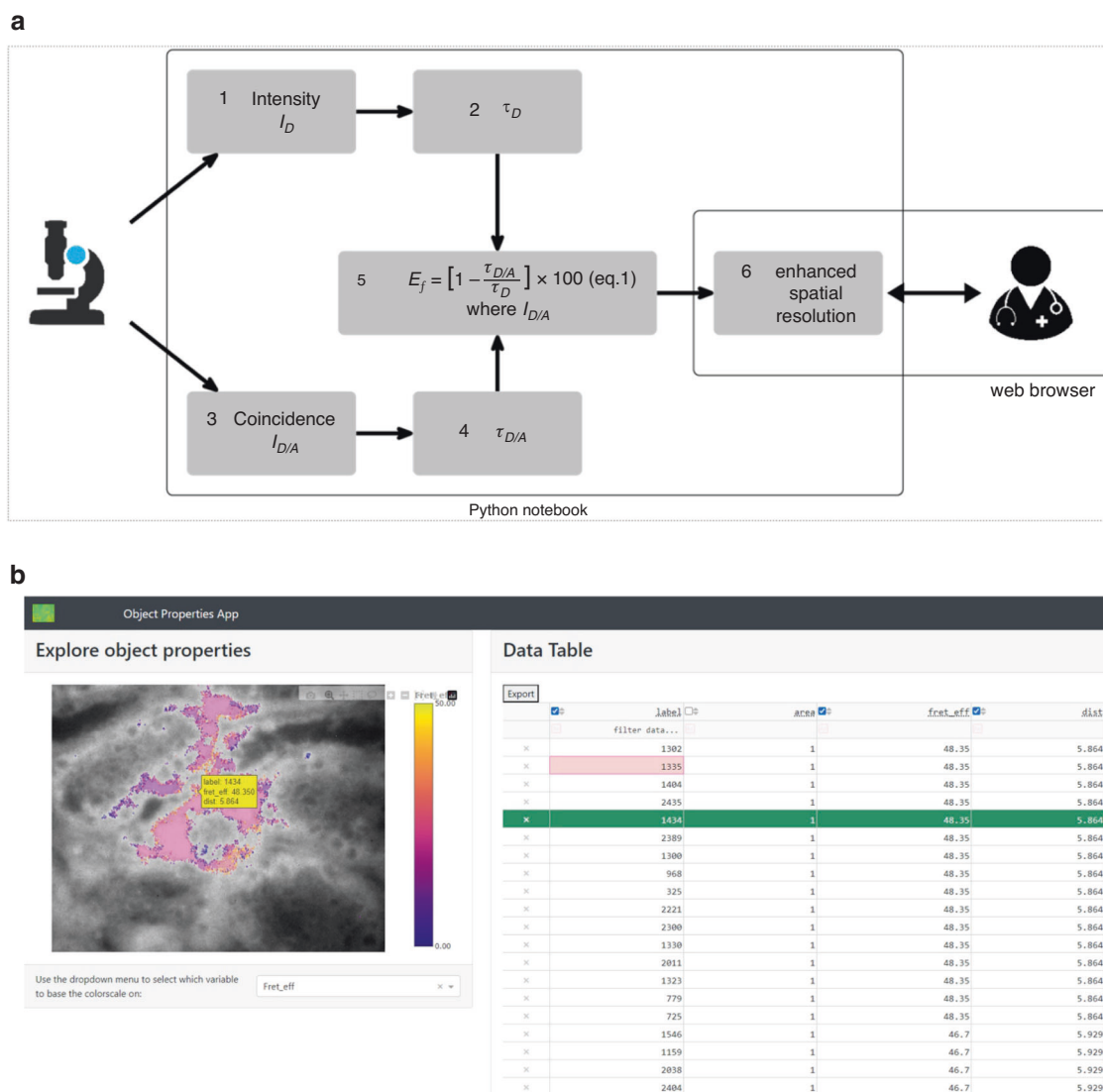


**Fig. 1 Schematic illustrating the computational process.** **a** Data flow illustrates the progression of information through key stages. Initially, input data fluorescence intensity ( $I_D$ ) and lifetime image  $\tau_D$  of the donor as well as the coincident images from the two-site analysis ( $I_{D/A}$ ) and  $\tau_{D/A}$  are stored on Google Drive. This data is retrieved during user execution of the GoogleColaboratory notebook. The notebook execution involves applying functions to process data and retain essential parameters for reproducibility. Finally, running the application enables user interaction with the FuncOmap interface. **b** Interactive FuncOmap in browser. The image on the left is of the coincidence of expressional and functional protein states coloured according to the level of activation as determined by the FRET-efficiency. Below the image, the user can select from a predefined set of thresholds that range from “background” to “3.5 times background,” with “background” set at twice the default value. To the right is a table that is completed to make Table 1.

## RESULTS

### Patient samples

A commercial 24 core tissue microarray (TMA) including samples of ccRCC, and their matched adjacent normal renal tissue was utilised. The normal tissue (B7) was used as a control and the HIF1 $\beta$ /HIF2 $\alpha$  and PD-1/PD-L1 activation states were compared to five different ccRCC patients (B5, A5, A2, A1 and B1). The patients B5, A5, A2 and A1 were Stage I and B1 was identified as Stage II. These samples were from male patients with a median age of 65 (range 42–77).

### aFRET quantifies HIF1 $\beta$ /HIF2 $\alpha$ interaction in normoxic and hypoxic conditions

Prior to determining the interaction of HIF1 $\beta$ /HIF2 $\alpha$  in patient samples we validated our approach in single cells (colorectal cells) under conditions of normoxia and hypoxia (1% O<sub>2</sub>, 48 h). Supplementary Fig. 1A shows under normoxic conditions HIF1 $\beta$

and HIF2 $\alpha$  do not interact (Median FRET efficiency of 3.95%), whereas there is a significant ( $p = 0.02$ ) interaction of 7.75% (median FRET efficiency) under hypoxic conditions. aFRET efficiency of 4% (see Eqs. 2, 3 in the “Methods”); thus any FRET value below 4% will be regarded as non-interactive. We have also determined whether there is a correlation between the HIF2 $\alpha$  expression levels and FRET efficiency. In normoxic conditions there is no correlation. Interestingly, under hypoxic conditions there is a negative correlation with the interactive state. Indicating that lower expression levels of HIF2 $\alpha$  correlate with higher interactive states of HIF1 $\beta$  and HIF2 $\alpha$ . We demonstrate that high expression levels of HIF2 $\alpha$  do not interact strongly with HIF1 $\beta$  (Supplementary Fig. 1B, C). Upon this cellular validation we sought to implement aFRET to patient samples to determine the interactive states of HIF1 $\beta$ /HIF2 $\alpha$  in ccRCC patients compared to normal renal tissue.



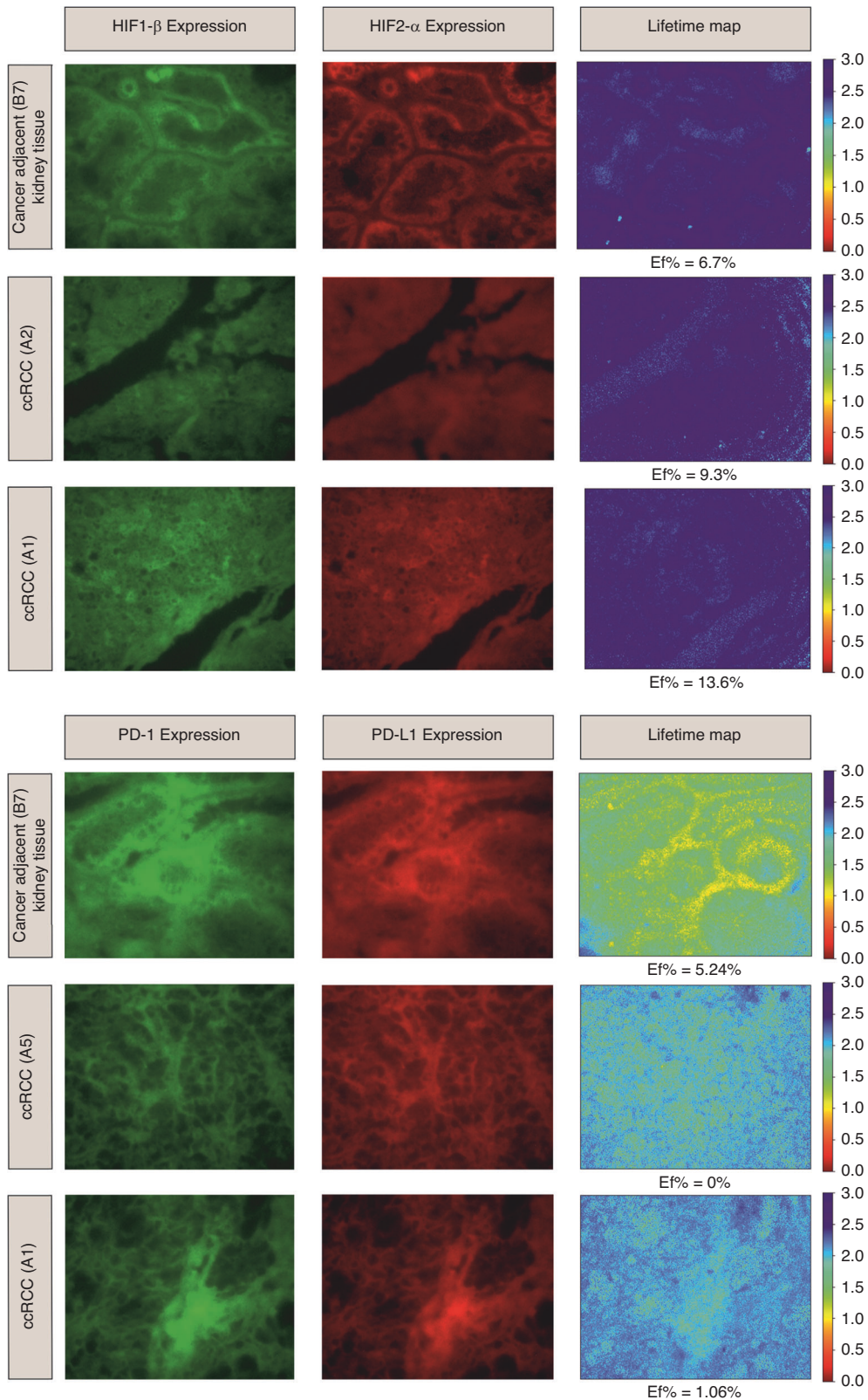


**Fig. 2 aiFRET quantifies HIF1 $\beta$ /HIF2 $\alpha$  and PD-1/PD-L1 interactive states in ccRCC patients.** The upper panel illustrates the expression of HIF1 $\beta$ /HIF2 $\alpha$ . HIF1 $\beta$  is the donor and HIF2 $\alpha$  is the acceptor. Their lifetime map is shown in the third column with the corresponding calculated median Ef. The median Ef for normal tissue was 6.70% and for patients A1 and A2 13.6% and 9.30% respectively. The lower panel shows the expression of PD-1 as the donor and the PDL1 the acceptor. The expression of PD-1/PD-L1 and their average lifetime map with their corresponding calculated median Ef is illustrated. The median Ef for normal tissue was 5.24% and for patients A1 and A2 is 1.06% and 0% respectively.

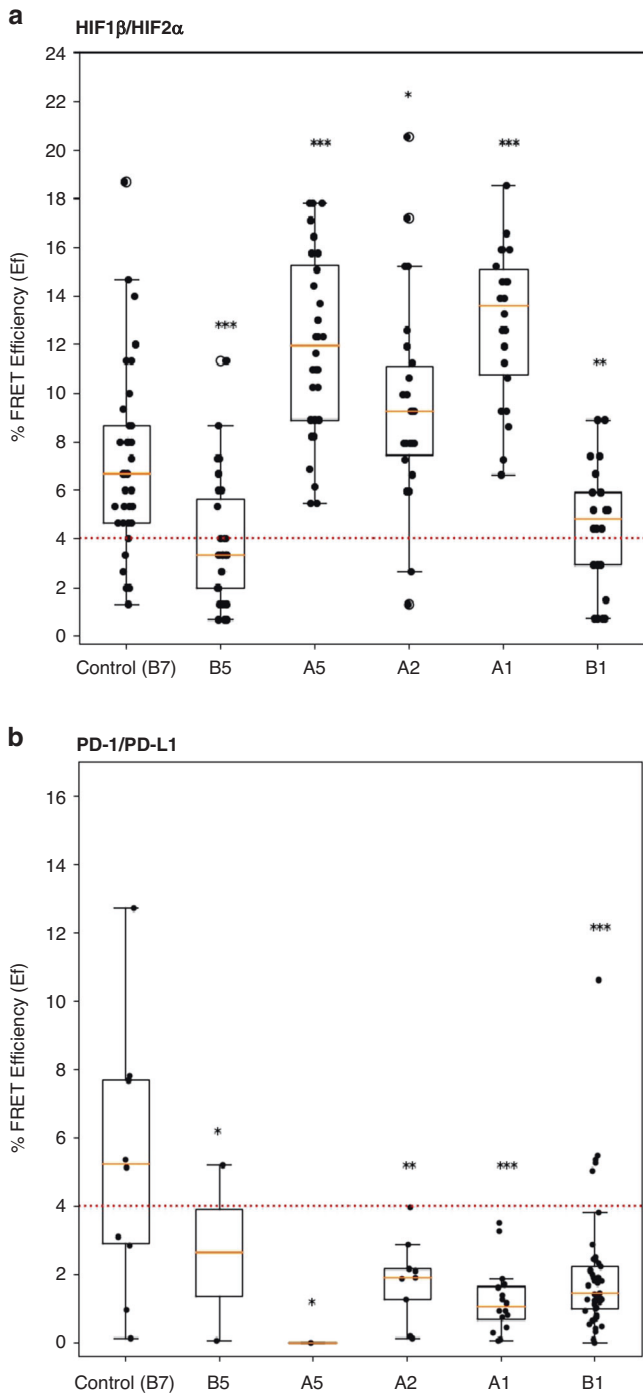


**Fig. 3 Statistical distribution of HIF1 $\beta$ /HIF2 $\alpha$  and PD-1/PD-L1 interactive states in ccRCC patients.** **a** Shows the HIF1 $\beta$ /HIF2 $\alpha$  box and whisker plots for each patient where the  $E_f$  distributions of HIF1 $\beta$ /HIF2 $\alpha$  were quantified for each core. **b** Demonstrates the corresponding box and whisker plots for each patient where the  $E_f$  distributions of PD-1/PD-L1 were quantified for each core. **a** HIF1 $\beta$ /HIF2 $\alpha$  The exact  $p$  values for each tumour core are: B5-  $p = 1.8 \times 10^{-4}$ , A5-  $p = 1.4 \times 10^{-6}$ , A2-  $p = 3 \times 10^{-2}$ , A1-  $p = 1.2 \times 10^{-6}$ , B1-  $p = 6 \times 10^{-3}$  **(b)** PD-1/PD-L1 the  $p$  values for each tumour core are: B5-  $p = 3.6 \times 10^{-1}$ , A5-  $p = 1.8 \times 10^{-1}$ , A2-  $p = 3.5 \times 10^{-2}$ , A1-  $p = 3 \times 10^{-3}$ , B1-  $p = 5 \times 10^{-3}$ . \* $p$  value of  $\geq 5 \times 10^{-2}$ , \*\* $p$  value in a range of  $5 \times 10^{-2}$  to  $5 \times 10^{-3}$ , \*\*\* $p$  value  $\leq 5 \times 10^{-3}$ . The points on each of the box and whisker plots in A and B correspond to distinct regions of interest (ROI) within each core.

### aiFRET quantifies HIF1 $\beta$ /HIF2 $\alpha$ and PD-1/PD-L1 interactive states in ccRCC patients

Figure 2 shows the expression of (a) HIF1 $\beta$ /HIF2 $\alpha$  and (b) PD-1/PD-L1. These are representative regions of interest from three different ccRCC patients. Two slides were used, one donor-only and one donor-acceptor. HIF1 $\beta$  was assessed on donor only and the second TMA slide was labelled with HIF1 $\beta$ /HIF2 $\alpha$ , with HIF2 $\alpha$  being the acceptor. Figure 2 (upper panel) illustrates the expression of HIF1 $\beta$ /HIF2 $\alpha$  and their lifetime map with the corresponding calculated median  $E_f$ . The median  $E_f$  for normal tissue was 6.70% and for patients A1 and A2 is 13.6% and 9.30%, respectively. Figure 3a shows the corresponding box and whisker plots for each patient where the  $E_f$  distributions of HIF1 $\beta$ /HIF2 $\alpha$  were quantified for each core.

PD-1/PD-L1 interactive states are shown in Fig. 2 (lower panel), where PD-1 is the donor and the PD-L1 the acceptor. The expression of PD-1/PD-L1 and their average lifetime map with their corresponding calculated median  $E_f$  is illustrated in Fig. 3b. The median  $E_f$  for normal tissue was 5.24% and for patients A1 and A2 is 1.06% and 0%, respectively.

The points on each of the box and whisker plots in Fig. 3a, b correspond to distinct regions of interest (ROI) within each core. Apart from the normal tissue in this incidence the patient samples with a FRET-Efficiency below 4% do not have an interactive state. As noted in the Introduction, the ROIs that indicate the interactive states of both HIF1 $\beta$ /HIF2 $\alpha$  and PD-1/PD-L1 cannot be mapped easily on the expression images of the HIF1 $\beta$  and PD-1. Therefore, to directly map the localisation of the interactive states, via  $E_f$  calculations, we devised another methodology and implemented this concept to provide location mapped  $E_f$  data.

### FuncOmap directly maps the interactive states of HIF1 $\beta$ /HIF2 $\alpha$ and PD-1/PD-L1 on the expression images of HIF1 $\beta$ and PD-1

Figure 4 shows the expression of HIF1 $\beta$ /HIF2 $\alpha$  and PD-1/PD-L1. The two-site assay illustrates regions of coincidence between HIF1 $\beta$ /HIF2 $\alpha$  in the control cancer adjacent normal kidney tissue (B7) and two additional ccRCC samples A5 and B5. The same cores were labelled for PD-1/PD-L1. The right-hand column of Fig. 4a, b illustrates FuncOmap. The pseudo-colour scale of the  $E_f$  ranges from 0.00% (purple) to 50% (yellow). FRET efficiency can only have a maximum value of 50% as the Förster radius,  $R_0$ , between the donor and acceptor fluorophores (Atto 488 and Alexa 594, respectively) is a constant value of 5.83 nm [14]. Equation (2) in M&M shows that protein-interaction distances, calculated from  $E_f$  only have a meaningful value between 5.83 to 10.00 nm (Table 1).

FuncOmap shows the pixel distribution of only the coincidence areas between HIF1 $\beta$ /HIF2 $\alpha$  and PD-1/PD-L1 in each representative region from the cores. Each pseudo-colour pixel within the coincidence area corresponds to the median  $E_f$ . Purple pixels/regions signify areas with low interaction to no interaction, while areas coloured in shades of orange and yellow denote regions with the highest interactive states. In the HIF1 $\beta$ /HIF2 $\alpha$  samples, the most intense interactive states were apparent in sample A5, while samples B7 and B5 exhibited low or no interaction respectively.

In PD-1/PD-L1 samples, A5 shows the least interaction. The control B7 and B5 exhibited the highest interactive regions. B5 high interaction states were dominant ROIs, whereas in B7, high interactive states were noticeable within specific pixels. This is the first time where the interactive states of PD-1/PD-L1 have been demonstrated in control renal tissue to this accuracy. This may be considered as the homeostatic interactive states of PD-1/PD-L1 in this type of renal tissue.

FuncOmap directly shows that the functional states do not correlate with the high fluorescent intensities (expression levels of HIF1 $\beta$  and PD-1).

Table 1 presents the coincidence regions where FRET-efficiencies were calculated, corresponding  $E_f$  and the related

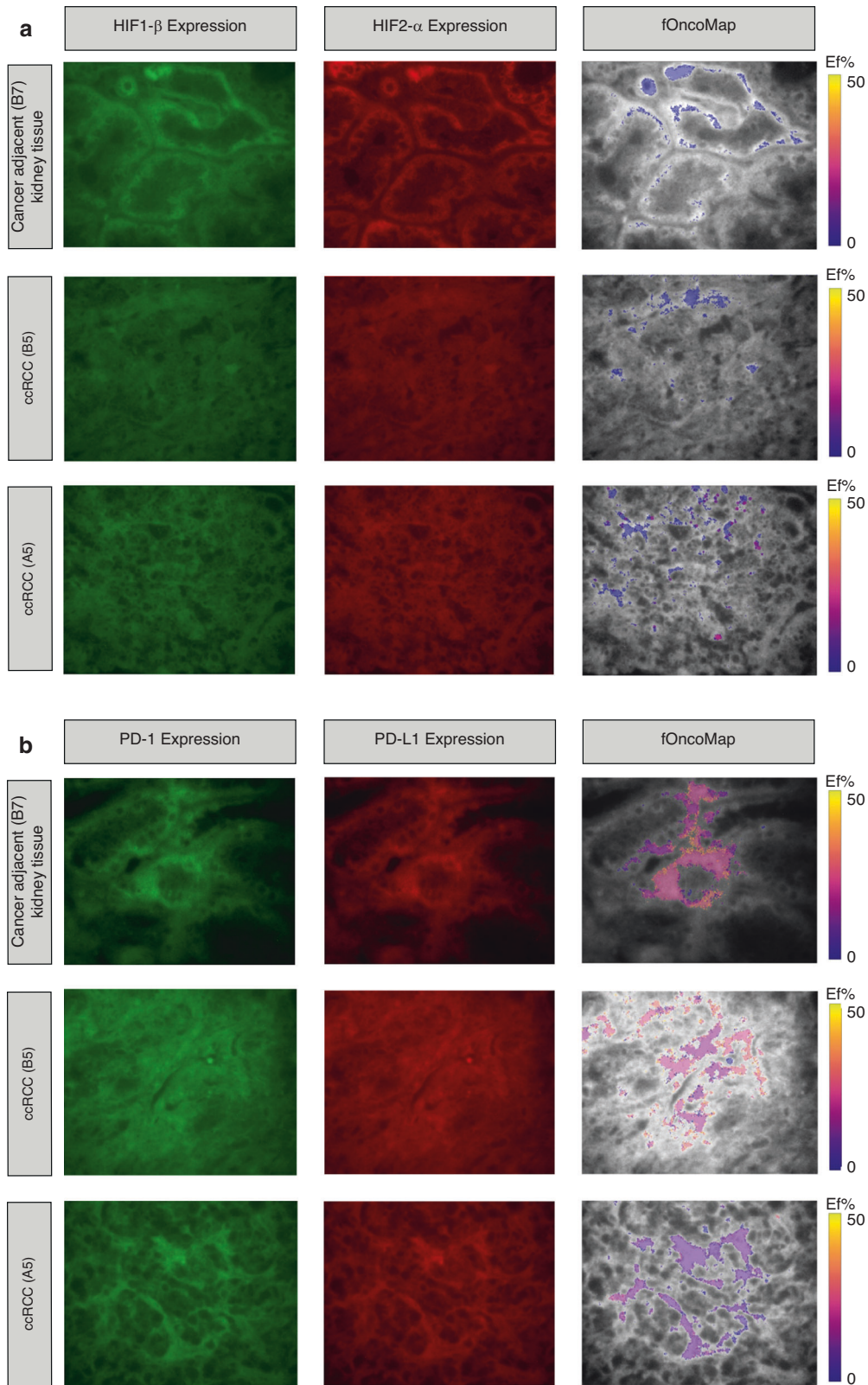


**Fig. 4** FuncOmap directly maps the interactive states of HIF1 $\beta$ /HIF2 $\alpha$  and PD-1/PD-L1 on the expression images of HIF1 $\beta$  and PD-1. **a** Shows the expression of HIF1 $\beta$ /HIF2 $\alpha$  and **(b)** PD-1/PD-L1. The two-site assay illustrates regions of coincidence between HIF1 $\beta$ /HIF2 $\alpha$  in the control cancer adjacent normal kidney tissue (B7) and 2 additional ccRCC samples A5 and B5. The same cores were labelled for PD-1/PD-L1. The right-hand column of **(a, b)** illustrate FuncOmap. The pseudo-colour scale of the Ef ranges from 0.00% (purple) to 50% (yellow).



**Table 1.** The quantifiable parameters obtained from regions of coincidence (two-site assay).

1A								
B7			B5			A5		
Coincidence region	Ef(%)	rnm	Coincidence region	Ef(%)	rnm	Coincidence region	Ef(%)	rnm
662	7.66	8.78	61	0.00		1307	21.10	7.23
672	4.95	9.49	103	0.00		1302	19.83	7.32
685	0.00		140	0.00		383	16.03	7.64
686	0.00		230	0.00		829	16.03	7.64
729	0.00		600	0.00		189	16.03	7.64
402	0.00		659	0.00		1299	16.03	7.64
712	0.00		220	0.00		235	15.41	7.70
950	0.00		632	0.00		1308	14.77	7.77
943	0.00		585	0.00		78	13.50	7.90
657	0.00		198	0.00		817	13.50	7.90
64	0.00		174	0.00		131	13.50	7.90
754	0.00		246	0.00		294	13.50	7.90
664	0.00		431	0.00		619	13.50	7.90
633	0.00		586	0.00		531	13.50	7.90
632	0.00		601	0.00		83	12.66	8.00
719	0.00		167	0.00		168	12.24	8.05
231	0.00		318	0.00		276	12.24	8.05
641	0.00		669	0.00		400	12.24	8.05
635	0.00		592	0.00		1273	12.24	8.05
636	0.00		162	0.00		826	12.24	8.05
637	0.00		452	0.00		187	12.24	8.05
638	0.00		80	0.00		12	12.24	8.05
639	0.00		199	0.00		822	12.24	8.05
640	0.00		277	0.00		679	12.24	8.05
634	0.00		242	0.00		733	11.40	8.16
1B								
B7			B5			A5		
Coincidence region	Ef(%)	rnm	Coincidence region	Ef(%)	rnm	Coincidence region	Ef(%)	rnm
233	48.35	5.86	551	16.39	7.61	92	8.60	8.60
984	22.28	7.14	1104	21.13	7.22	63	10.88	8.23
1273	23.41	7.07	1878	18.06	7.46	1250	10.08	8.35
24	21.54	7.19	1246	15.76	7.67	186	8.16	8.68
772	14.25	7.82	622	23.15	7.08	653	12.09	8.07
299	16.28	7.62	774	25.15	6.96	1064	10.56	8.28
442	19.10	7.38	249	23.63	7.05	823	9.22	8.49
1932	26.41	6.88	1612	13.92	7.86	505	7.72	8.77
1657	18.09	7.46	1288	26.31	6.89	110	8.34	8.65
384	16.50	7.60	586	16.99	7.56	639	11.19	8.19
648	26.62	6.87	1772	20.77	7.25	812	16.69	7.58
102	16.10	7.64	930	28.31	6.77	929	8.25	8.66
561	12.82	7.98	546	24.76	6.98	1113	4.28	9.74
905	12.03	8.08	373	23.96	7.03	57	0.00	
67	14.21	7.83	107	30.60	6.65	448	7.70	8.77
1750	18.15	7.46	1500	28.54	6.76	482	9.31	8.48



Table b. continued

1B								
B7			B5			A5		
Coincidence region	Ef(%)	rnm	Coincidence region	Ef(%)	rnm	Coincidence region	Ef(%)	rnm
1861	27.42	6.82	81	21.83	7.17	1274	8.32	8.65
548	23.38	7.07	1811	23.98	7.03	1360	6.13	9.14
1009	28.94	6.74	1187	0.00		1053	12.95	7.97
356	19.97	7.31	2232	28.32	6.77	949	6.49	9.05
1973	28.43	6.76	176	28.38	6.77	1405	12.38	8.04
1711	25.74	6.92	841	29.44	6.71	564	8.82	8.56
1919	14.73	7.77	261	15.74	7.67	1255	8.24	8.67
197	21.18	7.22	1155	20.38	7.28	1241	6.86	8.96
1454	29.85	6.69	2043	20.39	7.28	421	5.03	9.46

a Shows the coincidence regions where FRET-efficiencies were calculated, corresponding Ef and the related molecular distances for HIF1 $\beta$ /HIF2 $\alpha$ .

b Illustrates the coincidence regions where FRET-efficiencies were calculated, corresponding Ef and the related molecular distances for PD-1/PD-L1. It is of note that these values can be directly retrieved from FuncOmap.

molecular distances. It is of note that these values can be directly retrieved from FuncOmap.

Table 1A shows the FuncOmap for the HIF1 $\alpha$ /HIF2 $\beta$  interactions and Table 1B for PD-1/PD-L1. It can be clearly seen that all the molecular distances are greater than  $R_0$  (5.83 nm). The higher the Ef values the closer are the molecular interactions but the valid distances are between 5.83 to 10 nm .

## DISCUSSION

There is an urgent need for predictive biomarkers, particularly in ccRCC, where HIF2 $\alpha$  clinical trials and immunotherapy demonstrate an overall response rate of 40–50%. Further to this a 30–50% risk of severe adverse events is identified in ccRCC immunotherapy treated patients [15]. There are no approved genomic- or proteomic-based tools used in the clinic for the precise application of therapies. This is preventing the power of precision medicine from being achieved and produced ongoing problems with patient selection and treatment. Spatial profiling methods, such as immunohistochemistry, proximity ligation assays, Digital Spatial Profiling and single cell RNA sequencing, enhance the complexity of analyses that can be performed and data generated from formalin fixed, paraffin embedded (FFPE) patient samples. These methods can be time consuming, with costly sample preparations and only quantify RNA/protein expression levels and not their structural or post-translational modifications, parameters that are essential regulators of functional behaviour of proteins.

To achieve precision and the correct treatment of patients, posttranslational events and interactive states of proteins need to be quantified [4, 11, 12, 16].

Here we have developed a novel methodology for spatial functional proteomics, FuncOmap. This new direct analysis of functional states spatially maps the interactive events on the expression levels of proteins. This provides data for researchers and clinicians key to clinical decisions and molecular mechanistic understanding about the relationship between expression and interaction and highlights that expression does not correlate with regions with elevated interactive states. The heat map associated with FuncOmap facilitates the interpretation of functional heterogeneity, which is widely accepted as a key feature of therapeutic response, for clinicians and research histopathologists.

Furthermore, by exploiting this quantitative method we have also shown for the first time that we can determine the HIF complex interactive states in single cells under normoxic and hypoxic conditions. Our findings at the single cell level show that high expression levels of HIF2 $\alpha$  in hypoxic conditions do not interact strongly with HIF1 $\beta$ . Once again, illustrating that using changes in expression levels of HIF2 $\alpha$  is insufficient as a decision-making parameter.

In normal renal tissue and ccRCC patients show the basal level of PD-1/PD-L1 interactive state.

The varied response to HIF2 $\alpha$  inhibition in preclinical and clinical studies suggests that an assay of HIF2 $\alpha$  activation state (not just expression levels) is required as a more accurate predictive biomarker [8], enabling optimal use of HIF2 $\alpha$  inhibitors in the clinic [5]. Of course, other factors including genomic mutations, epigenetic changes, microenvironment may affect clinical outcome.

We have developed a novel biomarker assay which achieves this by quantifying the engagement of HIF2 $\alpha$  with HIF1 $\beta$  a determinant of activity [17, 18]. This assay may also be key for longitudinal clinical analysis of patient tumours whilst undergoing treatment with HIF2 $\alpha$  inhibitors to detect changes in sensitivity. This is key as mutations in HIF proteins that enable HIF2 $\alpha$  and HIF1 $\beta$  heterodimerisation in the presence of HIF2 $\alpha$  inhibitors are a mechanism of resistance [19, 20] that could be detected using this biomarker. Further to this a biomarker that accurately quantifies HIF2 $\alpha$ -HIF1 $\beta$  interaction could provide a useful tool to determine patients with solid tumours other than ccRCC that frequently exhibit hypoxia and may be sensitive to HIF2 $\alpha$  inhibitors. Thus, unlocking of the full potential of HIF2 $\alpha$  inhibitors for patient benefit

An interesting finding of this study is that we identify 2/5 patient tumour samples with below normal kidney tissue levels of HIF2 $\alpha$  and HIF1 $\beta$  interaction, including one which exhibited no interaction between HIF2 $\alpha$  and HIF1 $\beta$  in analysis by FuncOmap. This appears contrary to the widely held view that HIF2 $\alpha$  is the main driver of ccRCC [5]. This view is based upon the frequency of VHL mutations, found in >90% of ccRCC which led to HIF2 $\alpha$  stabilisation, and the HIF2 $\alpha$  functional in vitro investigations using cell lines and murine models of ccRCC which have limitations [21]. An alternative non-transcriptional role for HIF2 $\alpha$  could explain the

lack of HIF2 $\alpha$  and HIF1 $\beta$  interaction in these samples such as the role of HIF2 $\alpha$  in protein translation that has been described previously [22]. However, the data generated here suggests that further investigation in a larger sample population of ccRCC tumours is required, using functional proteomics approaches. This is likely key to understanding the inter- and intra- tumour heterogeneity of the role of HIF2 $\alpha$  in ccRCC.

There are several advantages of FuncOmap over box and whisker analyses, the main one being that all pixels of the coincident ROIs are considered, rather than calculating an average *Ef* of the coincident ROI. This provides higher precision in determining the functional states of the oncoproteins under investigation, in this case HIF1 $\alpha$ /HIF2 $\beta$  and PD-1/PD-L1. From FuncOmap, the molecular distances of HIF2 $\alpha$ /HIF1 $\beta$  and PD-1/PD-L1 can be directly obtained. The knowledge of molecular distances is important for determining mechanisms of drug-targeting. That is the precise variations of the distance (*r*), in Eq. (3), either in protein–protein interactions or changes of protein morphology, can determine whether drugs undergoing clinical trials, have affected the protein's dysfunctional state. This would be a major asset for determining the pharmacodynamics of newly developed drugs to prevent the high waste of funds with unsuccessful clinical trials.

Routine implementation of FuncOmap with appropriate functional biomarkers in the clinical arena is critically needed to improve overall survival in high-risk patients and significantly reduce the severe adverse events associated with broad use of different therapies.

Our goal is for FuncOmap to be used as a companion diagnostics in clinical trials as well as a generic clinical tool for determining the per-pixel functional states of proteins in any type of pathology.

#### DATA AVAILABILITY

The code for FuncOmap is available under licence for academic research at no cost. For further information, please contact the corresponding authors.

#### CODE AVAILABILITY

The code is available under licence for academic research at no cost and for commercial use subject to negotiation. For further information, please contact the corresponding authors JP and BL.

#### REFERENCES

1. Dutcher JP, Flippot R, Fallah J, Escudier B. On the shoulders of giants: the evolution of renal cell carcinoma treatment-cytokines, targeted therapy, and immunotherapy. *Am Soc Clin Oncol Educ Book*. 2020;40:1–18. [https://doi.org/10.1200/edbk\\_280817](https://doi.org/10.1200/edbk_280817).
2. Nickerson ML, Jaeger E, Shi Y, Durocher JA, Mahurkar S, Zaridze D, et al. Improved identification of von Hippel-Lindau gene alterations in clear cell renal tumors. *Clin Cancer Res*. 2008;14:4726–34. <https://doi.org/10.1158/1078-0432.Ccr-07-4921>.
3. Gerlinger M, Rowan AJ, Horswell S, Math M, Larkin J, Endesfelder D, et al. Intra-tumour heterogeneity and branched evolution revealed by multiregion sequencing. *N Engl J Med*. 2012;366:883–92. <https://doi.org/10.1056/NEJMoa1113205>.
4. Chen W, Hill H, Christie A, Kim MS, Holloman E, Pavia-Jimenez A, et al. Targeting renal cell carcinoma with a HIF-2 antagonist. *Nature*. 2016;539:112–7. <https://doi.org/10.1038/nature19796>.
5. Cho H, Du X, Rizzi JP, Liberzon E, Chakraborty AA, Gao W, et al. On-target efficacy of a HIF-2 $\alpha$  antagonist in preclinical kidney cancer models. *Nature*. 2016;539:107–11. <https://doi.org/10.1038/nature19795>.
6. Food U, Administration D. FDA approves belzutifan for cancers associated with von Hippel-Lindau disease. 2022. Available from: <https://www.fda.gov/drugs/resources-information-approved-drugs/fda-approves-belzutifan-cancers-associated-von-hippel-lindau-disease>.
7. Maxwell PH, Wiesener MS, Chang G-W, Clifford SC, Vaux EC, Cockman ME, et al. The tumour suppressor protein VHL targets hypoxia-inducible factors for oxygen-dependent proteolysis. *Nature*. 1999;399:271–5.
8. Cuvillier O. The therapeutic potential of HIF-2 antagonism in renal cell carcinoma. *Trans Androl Urol*. 2017;6:131.

9. Thouvenin J, Masson C, Boudier P, Maillet D, Kuchler-Bopp S, Barthélémy P, et al. Complete response in metastatic clear cell renal cell carcinoma patients treated with immune-checkpoint inhibitors: remission or healing? How to improve patients' outcomes? *Cancers*. 2023;15:793.
10. Hoeflin R, Harlander S, Schäfer S, Metzger P, Kuo F, Schönenberger D, et al. HIF-1 $\alpha$  and HIF-2 $\alpha$  differently regulate tumour development and inflammation of clear cell renal cell carcinoma in mice. *Nat Commun*. 2020;11:4111.
11. Sánchez-Magrner L, Miles J, Baker CL, Applebee CJ, Lee D-J, Elsheikh S, et al. High PD-1/PD-L1 checkpoint interaction infers tumor selection and therapeutic sensitivity to anti-PD-1/PD-L1 treatment. *Cancer Res*. 2020;80:4244–57.
12. Veeriah S, Lebouche P, de Naurois J, Jethwa N, Nye E, Bunting T, et al. High-throughput time-resolved FRET reveals Akt/PKB activation as a poor prognostic marker in breast cancer. *Cancer Res*. 2014;74:4983–95.
13. Otsu N. A threshold selection method from gray-level histograms. *IEEE Trans Syst Man Cybern*. 1979;9:62–6.
14. Wu P, Brand L. Resonance energy transfer: methods and applications. *Anal Biochem*. 1994;218:1–13.
15. Luke JJ, Rutkowski P, Queirolo P, Del Vecchio M, Mackiewicz J, Chiarion-Sileni V, et al. Pembrolizumab versus placebo as adjuvant therapy in completely resected stage IIB or IIC melanoma (KEYNOTE-716): a randomised, double-blind, phase 3 trial. *Lancet*. 2022;399:1718–29.
16. Miles J, Ward SG, Larjani B. The fusion of quantitative molecular proteomics and immune-oncology: a step towards precision medicine in cancer therapeutics. *FEBS Lett*. 2022;596:2721–35.
17. Tian H, McKnight SL, Russell DW. Endothelial PAS domain protein 1 (EPAS1), a transcription factor selectively expressed in endothelial cells. *Genes Dev*. 1997;11:72–82. <https://doi.org/10.1101/gad.11.1.72>.
18. Chilov D, Camenisch G, Kvietikova I, Ziegler U, Gassmann M, Wenger RH. Induction and nuclear translocation of hypoxia-inducible factor-1 (HIF-1): heterodimerization with ARNT is not necessary for nuclear accumulation of HIF-1 $\alpha$ . *J Cell Sci*. 1999;112:1203–12.
19. Courtney KD, Ma Y, Diaz de Leon A, Christie A, Xie Z, Woolford L, et al. HIF-2 complex dissociation, target inhibition, and acquired resistance with PT2385, a first-in-class HIF-2 inhibitor, in patients with clear cell renal cell carcinoma. *Clin Cancer Res*. 2020;26:793–803.
20. Toledo RA, Jimenez C, Armaiz-Pena G, Arenillas C, Capdevila J, Dahia PL. Hypoxia-Inducible Factor 2 alpha (HIF2 $\alpha$ ) inhibitors: targeting genetically driven tumor hypoxia. *Endocrine Rev*. 2023;44:312–22.
21. Choi WSW, Boland J, Lin J. Hypoxia-inducible factor-2 $\alpha$  as a novel target in renal cell carcinoma. *J Kidney Cancer VHL*. 2021;8:1.
22. Uniacke J, Holterman CE, Lachance G, Franovic A, Jacob MD, Fabian MR, et al. An oxygen-regulated switch in the protein synthesis machinery. *Nature*. 2012;486:126–9.

#### ACKNOWLEDGEMENTS

We would like to thank Professors Gail McConnell and Robert Insall for critically reading the manuscript. We are grateful to Alexander Fezovich (Alan McIntyre Laboratory) for the performing the colorectal cell work.

#### AUTHOR CONTRIBUTIONS

ES- wrote first draft, devised the FuncOmap algorithm, generated and interpreted some of the results, helped to acquire the tissue and cell images on mFLIM. CA- acquired the tissue images, trained ES to acquire the images on mFLIM, helped with interpretation of results. AM- supervised the HIF single cell sample preparations, edited the final article, scientific discussions. JP- supervised ES and the generation of the FuncOmap algorithm, wrote the computation science sections of the paper, edited final article. BL- supervised the whole project and ES, interpreted all the results, generated the idea of how to implement functional state on expression state of proteins, thus the type of computation that was required, wrote the definitive version of the article.

#### FUNDING

The work was supported by funding from MRC (MR/P010334/1) awarded to AM and the Alumni Funds University of Bath awarded to BL. Elena Safrygina is supported by a studentship from the UKRI Centre for Doctoral Training in Accountable Responsible and Transparent Artificial Intelligence (ART-AI) [grant number EP/S023437/1].

#### COMPETING INTERESTS

BL is an Associate Editor for BJC Reports.

**CONSENT TO PARTICIPATE**

All Authors have read the final version of the publication and provide full consent for its publication.

**ADDITIONAL INFORMATION**

**Supplementary information** The online version contains supplementary material available at <https://doi.org/10.1038/s44276-023-00033-7>.

**Correspondence** and requests for materials should be addressed to Julian Padget or Banafshé Larijani.

**Reprints and permission information** is available at <http://www.nature.com/reprints>

**Publisher's note** Springer Nature remains neutral with regard to jurisdictional claims in published maps and institutional affiliations.



**Open Access** This article is licensed under a Creative Commons Attribution 4.0 International License, which permits use, sharing, adaptation, distribution and reproduction in any medium or format, as long as you give appropriate credit to the original author(s) and the source, provide a link to the Creative Commons licence, and indicate if changes were made. The images or other third party material in this article are included in the article's Creative Commons licence, unless indicated otherwise in a credit line to the material. If material is not included in the article's Creative Commons licence and your intended use is not permitted by statutory regulation or exceeds the permitted use, you will need to obtain permission directly from the copyright holder. To view a copy of this licence, visit <http://creativecommons.org/licenses/by/4.0/>.

© The Author(s) 2024, corrected publication 2024